RSC Advances

PAPER

View Article Online
View Journal | View Issue

Cite this: *RSC Adv.*, 2019, **9**, 891

Luminescence properties in relation to controllable morphologies of $Ba_3[Ge_2B_7O_{16}(OH)_2](OH)(H_2O):Eu^{3+}$ and its thermal conversion product $Ba_3Ge_2B_6O_{16}:Eu^{3+}$†

Pan Liang

Received 18th October 2018
Accepted 15th December 2018

DOI: 10.1039/c8ra08636b

rsc.li/rsc-advances

Three types of morphologies of Eu^{3+}-doped $Ba_3[Ge_2B_7O_{16}(OH)_2](OH)(H_2O)$ phosphors were obtained *via* hydrothermal reactions by different kinds of raw materials. In addition, $Ba_3Ge_2B_6O_{16}:Eu^{3+}$ phosphors were obtained by calcining the precursor $Ba_3[Ge_2B_7O_{16}(OH)_2](OH)(H_2O):Eu^{3+}$. The structure and morphology of the obtained samples were characterized by XRD, EDS, FT-IR, TG-DTA, SEM and HRTEM. Herein, the effects of the synthesis parameters, including the reaction temperature, boron sources and the rare earth doping dosage, on the photoluminescence (PL) properties of $Ba_3[Ge_2B_7O_{16}(OH)_2](OH)(H_2O)$ were investigated in detail. The lifetime and absolute quantum yield (QY) of different morphologies of $Ba_3[Ge_2B_7O_{16}(OH)_2](OH)(H_2O):Eu^{3+}$ were also measured. The PL properties of the $Ba_3Ge_2B_6O_{16}:Eu^{3+}$ phosphor prepared by the precursor calcination method compared with those prepared by the high-temperature solid-state method are discussed.

Introduction

In the past, many borates were chosen as host lattices for phosphors because of their large band gap, high thermal stability, high luminescence efficiency and low cost.[1–5] Borogermanates, as one kind of borates, have different chemical compositions and structures derived from the flexible coordination geometries for both B and Ge atoms. The use of borogermanates with alkali, alkaline-earth and transition metals has gained considerable interest due to their excellent Second Harmonic Generation (SHG) coefficients, high optical-damage thresholds, photocatalytic applications and excellent thermal stability.[6–12] Moreover, borogermanates can be a promising luminescence host material. The luminescence properties of some rare earth borogermanates doped with different kinds of rare earth metals, such as $LaBGeO_5$, $EuGeBO_5$ and $Ln_2GeB_2O_2$,have been studied.[13–17]

The properties and applications of luminescent materials are strongly dependent on their chemical composition, crystal structure, size and morphology.[18] For instance, Zhu *et al.* have investigated the effects of trace alkali metal ion (Li^+, Na^+, K^+) doping on the morphology and photoluminescence properties, and they deemed that the morphology influences the luminescence properties by geometric effects. Scattering occurs more frequently because of the distinctive particle shapes and surface roughness, which results in less absorption and decreased luminous efficiency. After doping with the alkali metal, the particle surface becomes smooth and the particle size gets reduced, meanwhile decreasing the number of surface-related defects. It leads to weaker nonradiative transitions and longer decay time afterwards.[19] Li *et al.* have developed a series of one-dimensional $Zn_2GeO_4:Mn^{2+}$ phosphors with H_2O/EG as a solvent; they thought that the smaller particle size generally presents larger surface area and more defects in the host matrix, which may result in a weaker luminescence. Therefore, the $Zn_2GeO_4:Mn^{2+}$ nanobundles exhibit broader diameters and larger particle size, which induces lower surface area and leads to fewer defects and stronger luminescence.[20] Wang *et al.* have synthesized various Tb^{3+}-doped calcium borate micro/nanostructures, such as $Ca_4B_{10}O_{19}\cdot 7H_2O$ micro/nanoflakes, $Ca_2B_2O_5\cdot H_2O$ micro/nanorods, hierarchical micro–nanostructures, monodispersed nanobelts and $Ca_3B_2O_6$ polyhedron-type particles, *via* a facile hydrothermal method. The influence of the morphology and crystalline phase on the photoluminescence of Tb^{3+} ions in the borate micro-nanostructures was investigated. These results indicate that both the crystal lattice and the morphology have important influence on the emission of Tb^{3+}.[21] Zhu *et al.* have synthesized red phosphors of the Mn^{4+}-doped dodec-fluoride $Li_3Na_3Ga_2F_{12}:Mn^{4+}$ (LNGF:Mn) with various morphologies. The micro-morphologies of LNGF:Mn change from flake to cube and to polyhedron shapes with an increase in the HF concentration from 10 to 40 wt%. The luminescence intensity of LNGF:Mn increases linearly with

Department of Chemistry & Chemical Engineering, Shaanxi Xueqian Normal University, Xi'an 710100, P. R. China. E-mail: B14159@snnu.edu.cn

† Electronic supplementary information (ESI) available. See DOI: 10.1039/c8ra08636b

the increase in the HF concentration, which might be jointly caused by the formation of higher concentrations of luminescence centers and the polyhedrons has better crystallinity.[22] Hence, controlling the size and morphology of the phosphors precisely enables us to manipulate their properties as desired. In addition, the properties are usually dependent on the preparation methods and the reaction parameters. To date, many researchers have prepared rare earth ion-doped inorganic phosphors of different morphologies only by changing the raw reaction materials. For instance, Ding *et al.* have prepared Eu^{3+}-doped $InBO_3$ phosphors with four kinds of morphologies (microsphere, flat microsphere with a hole, octahedron and oblique hexahedron) *via* a facile flux method only by adjusting the kinds of reaction boron source materials;[23] Yue *et al.* have prepared Ln^{3+} (Ln = Tb, Eu)-doped zinc phosphate with different morphologies (regular nanosheet, fractured nanosheet, irregular nanosheet, and self-assembly microflower) only by altering the phosphate sources;[24] Zou *et al.* have synthesized YBO_3:Eu^{3+} phosphors with different morphologies (flower-like and nano-scaled particles) by simply adjusting the B^{3+} sources.[25]

$Ba_3[Ge_2B_7O_{16}(OH)_2](OH)(H_2O)$ and $Ba_3Ge_2B_6O_{16}$ are potential SHG materials.[26] However, there are no reports on the use of these two barium borogermanates as matrix luminescence materials. In this paper, we first prepared Eu^{3+}-doped $Ba_3[Ge_2B_7O_{16}(OH)_2](OH)(H_2O)$:$Eu^{3+}$ with rhombohedron-like morphology, thorn-ball-like morphology and hexagonal-flakes-like morphology by the hydrothermal method and we also prepared $Ba_3Ge_2B_6O_{16}$:Eu^{3+} phosphor by the precursor calcination method. The effects of the experimental parameters, including the rare earth doping dosage, boron sources, and reaction time, on the photoluminescence (PL) properties of $Ba_3[Ge_2B_7O_{16}(OH)_2](OH)(H_2O)$ were investigated in detail. In addition, the PL properties of $Ba_3Ge_2B_6O_{16}$:Eu^{3+} prepared by two methods are compared and discussed.

Experimental

Synthesis of samples

Preparation of $Ba_3[Ge_2B_7O_{16}(OH)_2](OH)(H_2O)$:$Eu^{3+}$ phosphors. All the reagents were of analytical grade and used directly without further purification.

In a typical procedure, the raw materials $BaCO_3$ (0.7425 mmol, 0.1465 g), Eu_2O_3 (0.0038 mmol, 0.0013 g), GeO_2 (0.5 mmol, 0.052 g), H_3BO_3 (1.75 mmol, 0.108 g) and H_2O (2.0 mL) were sealed in an autoclave with a Teflon lining. The autoclave was then placed in an oven and maintained at 200 °C for 4 days. After cooling to room temperature, the products were obtained by filtering, washing with deionized water and ethanol for several times, and drying at 60 °C for 12 h.

For the synthesis of $Ba_3[Ge_2B_7O_{16}(OH)_2](OH)(H_2O)$:$Eu^{3+}$ phosphors of other morphologies, the procedures were the same as stated above except that the boron source of H_3BO_3 was replaced with an equal amount of $NH_4B_5O_8\cdot4H_2O$ (0.35 mmol, 0.0953 g) and $Na_2B_4O_7\cdot10H_2O$ (0.4375 mmol, 0.1669 g), respectively.

Preparation of $Ba_3Ge_2B_6O_{16}$:Eu^{3+} phosphors. $Ba_3Ge_2B_6O_{16}$:Eu^{3+} phosphors were prepared by calcining the $Ba_3[Ge_2B_7O_{16}(OH)_2](OH)(H_2O)$:$Eu^{3+}$ precursor at 900 °C for 5 h in air.

For comparison, the sample $Ba_3Ge_2B_6O_{16}$:Eu^{3+} was also synthesized by a conventional high-temperature solid-state reaction method at 900 °C for 5 h according to the literature.[26]

Characterization

The structures of the prepared samples were characterized by X-ray powder diffraction (XRD, Rigaku D/MAX-C, Cu Kα radiation at 40 kV and 30 mA), FT-IR spectroscopy (recorded over the 400 to 4000 cm^{-1} region using a Nicolet NEXUS 670 spectrometer with KBr pellets at room temperature), TG-DTA (TA-SDT Q600, in a N_2 atmosphere at a heating rate of 10 K min^{-1}), and energy-dispersive X-ray spectrometer (EDS, Hitachi, JEOL-6700F). The morphology and size of the product were investigated by scanning electron microscopy (SEM, Philips-FEI, Quanta 200). The inter-planar spacing of the crystal stripes of the sample was characterized by field transmittance electron microscopy (TEM) (Tecnai G2 F20, FEI). The photoluminescence (PL) spectra were recorded at room temperature using a molecular fluorescence spectrometer (FL-4600, Hitachi) equipped with a 150 W xenon lamp as an excitation source. The lifetime was recorded using an FLS920P Edinburgh Analytical Instrument apparatus equipped with a 450 W xenon lamp and a μF900H high-energy micro-second flash lamp as the excitation sources. The absolute photoluminescence quantum yield (QY) was measured by a Hamamatsu (C9920-02G) analytical instrument apparatus using an integrating sphere.

Results and discussion

Structure identification of the samples

Fig. 1A shows the powder XRD pattern of the as-synthesized $Ba_3[Ge_2B_7O_{16}(OH)_2](OH)(H_2O)$:$Eu^{3+}$ with three kinds of boron sources (a) H_3BO_3, (b) $NH_4B_5O_8\cdot4H_2O$ and (c) $Na_2B_4O_7\cdot10H_2O$, and $Ba_3[Ge_2B_7O_{16}(OH)_2](OH)(H_2O)$ single-crystal structure simulated pattern. Fig. 1B shows the powder XRD pattern of $Ba_3Ge_2B_6O_{16}$:Eu^{3+} samples with two different methods: (a) calcination precursor method and (b) high temperature solid-state method, and $Ba_3Ge_2B_6O_{16}$ single-crystal structure simulated pattern. It can be observed that all the diffraction peaks in Fig. 1A and B are in good agreement with the monoclinic phase $Ba_3[Ge_2B_7O_{16}(OH)_2](OH)(H_2O)$ and the triclinic phase $Ba_3Ge_2B_6O_{16}$, respectively. No impurity peaks were observed. A small amount of doped Eu^{3+} ions did not cause any significant change in the crystal structure of the host $Ba_3[Ge_2B_7O_{16}(OH)_2](OH)(H_2O)$ and $Ba_3Ge_2B_6O_{16}$.

Fig. S1a and b† show the EDS pattern of $Ba_3[Ge_2B_7O_{16}(OH)_2](OH)(H_2O)$:$Eu^{3+}$ and $Ba_3Ge_2B_6O_{16}$:Eu^{3+}, respectively. The EDS patterns clearly indicate that the two obtained samples contain B, O, Ba, Ge and Eu elements, and there are no other impurity element peaks.

Fig. 2a and b show the FT-IR spectra of $Ba_3[Ge_2B_7O_{16}(OH)_2](OH)(H_2O)$:$Eu^{3+}$ and $Ba_3Ge_2B_6O_{16}$:Eu^{3+}, respectively. In Fig. 2a, the bands at 3427 cm^{-1}, 3167 cm^{-1} and 1629 cm^{-1} are

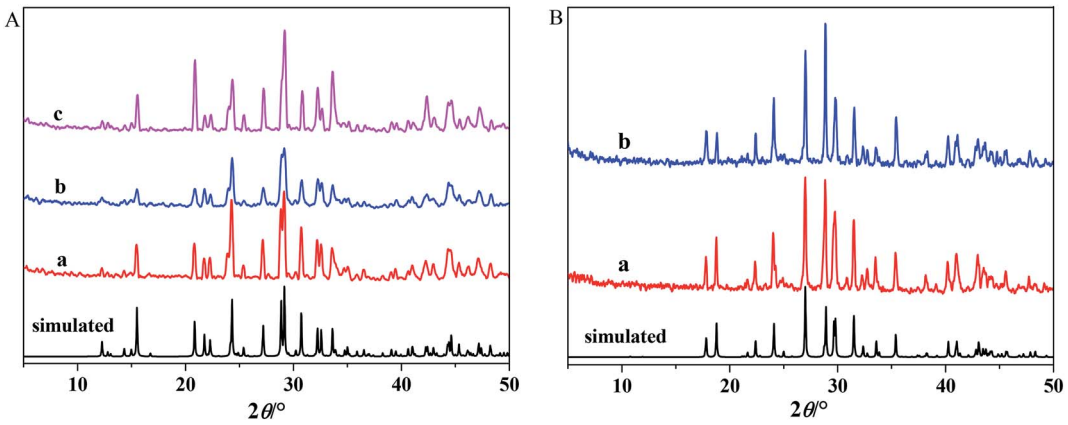

Fig. 1 (A) The powder XRD pattern of $Ba_3[Ge_2B_7O_{16}(OH)_2](OH)(H_2O):Eu^{3+}$ with different synthetic materials: (a) H_3BO_3, (b) $NH_4B_5O_8\cdot4H_2O$, and (c) $Na_2B_4O_7\cdot10H_2O$. (B) The XRD pattern of $Ba_3Ge_2B_6O_{16}:Eu^{3+}$ obtained by different methods: (a) calcination precursor method and (b) high temperature solid-state method.

attributed to the stretching and bending vibrations of O–H. The absorption peak at 1383 cm^{-1} can be assigned to the asymmetrical stretching of B(3)–O. The peak at 1260 cm^{-1} is attributed to the in-plane bending vibration of B–O–H. The peaks at 1130 cm^{-1} and 918 cm^{-1} are attributed to the symmetric stretching of B(4)–O. The peaks at 870 cm^{-1} and 836 cm^{-1} are attributed to the asymmetric stretching of Ge(4)–O. The peak at 487 cm^{-1} is attributed to the flexural vibration of Ge(4)–O. The peaks at 657 cm^{-1} and 576 cm^{-1} are attributed to the flexural vibration of B(3)–O and B(4)–O. In Fig. 2b, the absorption peaks at 1370 cm^{-1} and 1260 cm^{-1} can be assigned to the asymmetrical stretching of B(3)–O. The peaks at 1062 cm^{-1} and 924 cm^{-1} are attributed to the symmetric stretching of B(4)–O. The peaks at 871 cm^{-1}, 832 cm^{-1} and 773 cm^{-1} are assigned to the asymmetric stretching of Ge(4)–O. The peak at 459 cm^{-1} is assigned to the flexural vibration of Ge(4)–O. The peaks at 610 cm^{-1} and 583 cm^{-1} are assigned to the flexural vibration of B(3)–O and B(4)–O. The corresponding absorption bands of $Ba_3[Ge_2B_7O_{16}(OH)_2](OH)(H_2O):Eu^{3+}$ and $Ba_3Ge_2B_6O_{16}:Eu^{3+}$ are similar to those reported in the literature, respectively.[26] Therefore, we conclude that we obtained the $Ba_3[Ge_2B_7O_{16}(OH)_2](OH)(H_2O):Eu^{3+}$ and $Ba_3Ge_2B_6O_{16}:Eu^{3+}$ phosphors.

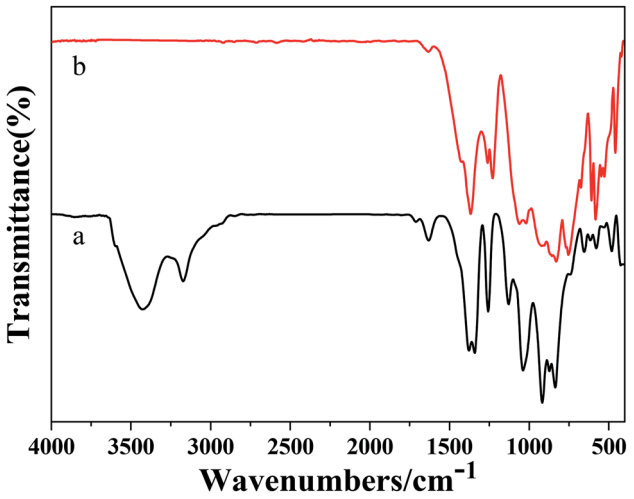

Fig. 2 FT-IR spectrum of samples: (a) $Ba_3[Ge_2B_7O_{16}(OH)_2](OH)(H_2O):Eu^{3+}$ and (b) $Ba_3Ge_2B_6O_{16}:Eu^{3+}$.

Fig. S2† shows the simultaneous TG-DTA curves of $Ba_3[Ge_2B_7O_{16}(OH)_2](OH)(H_2O):Eu^{3+}$. TG studies indicate that there is no weight loss before 673 K, and it exhibits the initial step of weight loss in the range of 673–1073 K, which corresponds to the release of 2.5 water molecules per formula unit. The observed weight loss of 4.8% matches well with the theoretical calculation result (4.7%). This assignment is also in agreement with the endothermic peak at 883 K in the DTA diagram. This results indicated that $Ba_3[Ge_2B_7O_{16}(OH)_2](OH)(H_2O):Eu^{3+}$ is thermally stable upto 673 K.

Fig. 3 shows the SEM images of the as-synthesized $Ba_3[Ge_2B_7O_{16}(OH)_2](OH)(H_2O):Eu^{3+}$ samples with different boron sources as raw reaction materials. It is apparent that $Ba_3[Ge_2B_7O_{16}(OH)_2](OH)(H_2O):Eu^{3+}$ synthesized with H_3BO_3 as the boron source displays rhombohedron-like morphology with an edge of about 2 μm (shown in Fig. $3a_1$ and a_2). $Ba_3[Ge_2B_7O_{16}(OH)_2](OH)(H_2O):Eu^{3+}$ synthesized with $NH_4B_5O_8\cdot4H_2O$ as the boron source displays uniformly sized thorn-ball-like morphology, which is constructed by lots of nano-particles, with diameters of about 10 μm (shown in Fig. $3b_1$ and b_2). $Ba_3[Ge_2B_7O_{16}(OH)_2](OH)(H_2O):Eu^{3+}$ synthesized with $Na_2B_4O_7\cdot10H_2O$ as the boron source displays hexagonal-flake morphology with an edge of about 1 μm and a thickness of about 100 nm (shown in Fig. $3c_1$ and c_2). Different morphologies can be obtained by using different boron sources. When the different boron sources were introduced into the reaction system, the pH values and the existing cations were different; the acidity of H_3BO_3 is lower than those of $NH_4B_5O_8\cdot4H_2O$ and $Na_2B_4O_7\cdot10H_2O$. The pH value can affect the kinds and qualities of the absorbed ions on the surface of the crystal.[23] Thus, the surface energy of the crystal is different. According to the Gibbs–Curie–Wulff theorem, the growth rates on different surface facets are dominated by the surface energy.[27] As a result, the different growth rates direct the different growth directions

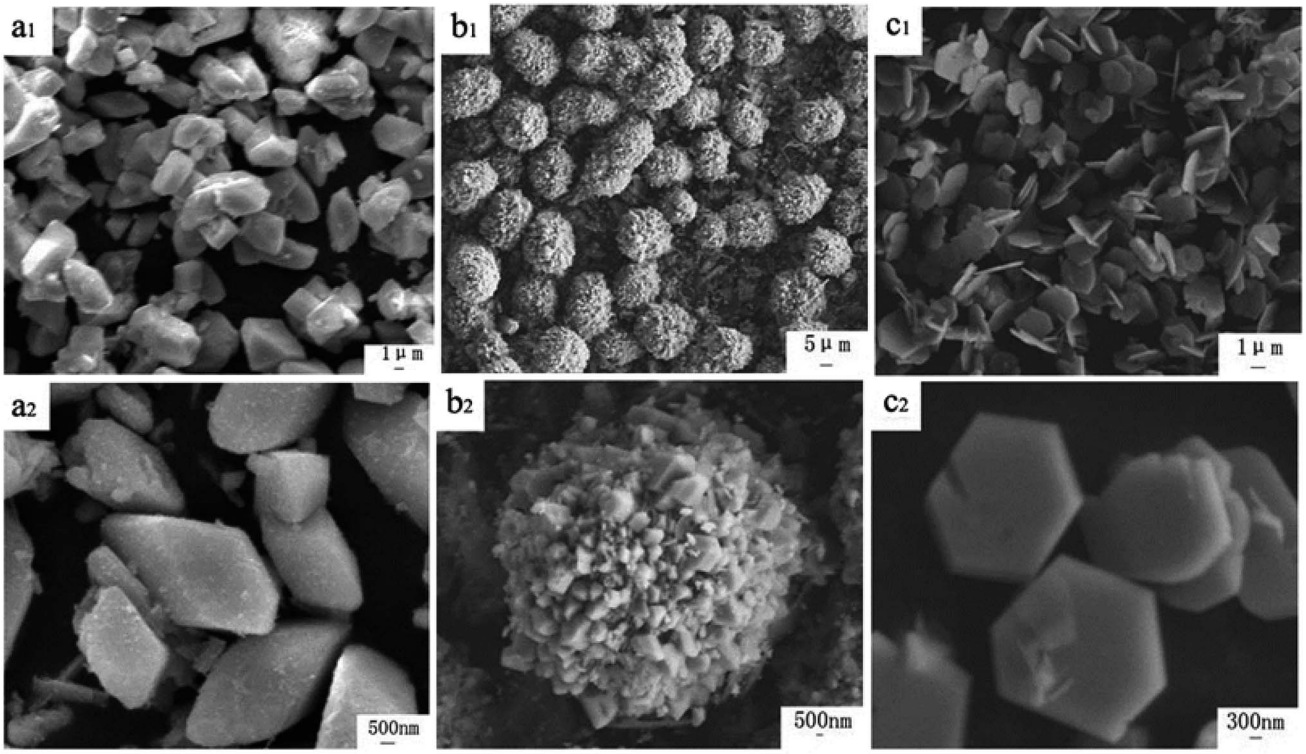

Fig. 3 SEM images of $Ba_3[Ge_2B_7O_{16}(OH)_2](OH)(H_2O):Eu^{3+}$ with different raw materials: (a_1 and a_2) H_3BO_3, (b_1 and b_2) $NH_4B_5O_8\cdot 4H_2O$ and (c_1 and c_2) $Na_2B_4O_7\cdot 10H_2O$.

and further direct the different final morphology of the obtained samples.

HREM images of the three different morphologies of $Ba_3[Ge_2B_7O_{16}(OH)_2](OH)(H_2O):Eu^{3+}$ samples are displayed in Fig. 4. The inter-planar spacing of the rhombohedron-like morphology sample is 4.258 Å, which is consistent with the *d* value (4.258 Å) of (020) faces in the $Ba_3[Ge_2B_7O_{16}(OH)_2](OH)(H_2O)$ crystal. The inter-planar spacing of the thorn-ball-like morphology sample is 3.268 Å, which is very close to the *d* value (3.274 Å) of (221) faces in $Ba_3[Ge_2B_7O_{16}(OH)_2](OH)(H_2O)$ crystal. The inter-planar spacing of the hexagonal-flake morphology sample is 2.840 Å, which is close to the *d* value (2.855 Å) of (222) faces in the $Ba_3[Ge_2B_7O_{16}(OH)_2](OH)(H_2O)$ crystal.

Fig. S3† shows the SEM images of $Ba_3Ge_2B_6O_{16}:Eu^{3+}$ prepared by different reaction methods: (a) precursor method; and (b) solid-state method. It can be seen that the $Ba_3Ge_2B_6O_{16}:Eu^{3+}$ sample prepared by the precursor method exhibits porous surface block structure. In addition, the $Ba_3Ge_2B_6O_{16}:Eu^{3+}$ sample prepared by the solid-state method exhibits irregular block structure.

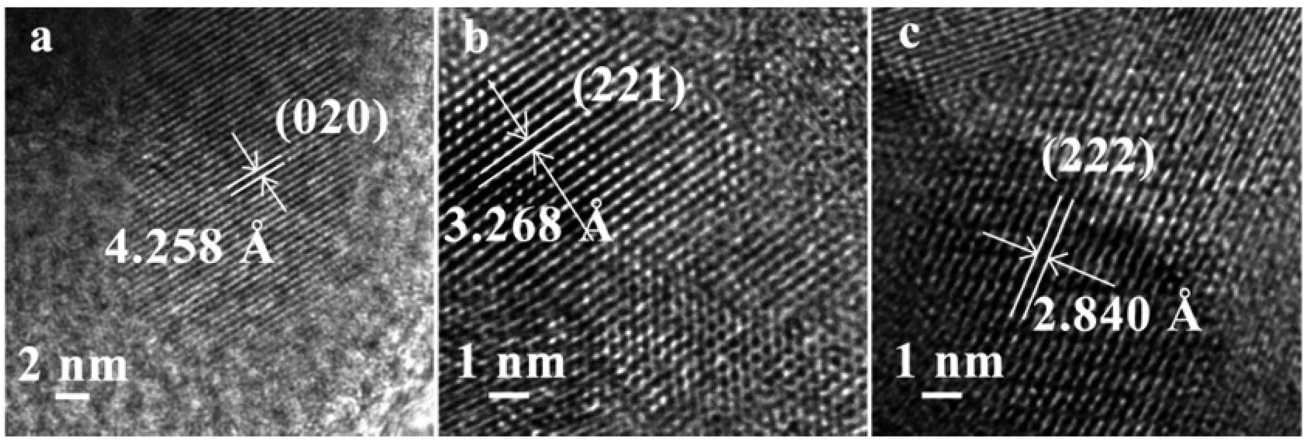

Fig. 4 High-resolution TEM images of $Ba_3[Ge_2B_7O_{16}(OH)_2](OH)(H_2O):Eu^{3+}$ with different morphologies: (a) rhombohedron-like morphology, (b) thorn-ball-like morphology and (c) hexagonal-flake morphology.

Photoluminescence properties

Effect of doped Eu^{3+} concentration on the PL intensity of $Ba_3[Ge_2B_7O_{16}(OH)_2](OH)(H_2O):Eu^{3+}$. The PLE and PL spectra under UV excitation for the hexagonal-flake morphology of $Ba_3[Ge_2B_7O_{16}(OH)_2](OH)(H_2O):xEu^{3+}$ ($x = 1\%$, 3%, 5%, and 7%, mole ratio) were recorded at room temperature. The excitation spectra of $Ba_3[Ge_2B_7O_{16}(OH)_2](OH)(H_2O):Eu^{3+}$, recorded at an emission wavelength of 615 nm, are shown in Fig. 5 (inset). The excitation spectra exhibits a strong charge transfer band (CTB) from the 2p orbital of O^{2-} to the 4f orbital of Eu^{3+} with a maximum peak at about 242 nm. Other weak peaks are attributed to the f–f transitions of Eu^{3+}.[28] Fig. 5 shows the emission spectra of the samples with different concentrations of doped Eu^{3+} upon excitation at 242 nm wavelength. No remarkable differences in the spectroscopic characteristics were observed upon excitation at the same wavelength when different concentrations of Eu^{3+} ions were doped. The peaks at the 589 nm and 600 nm are due to the split sublevels of the magnetic dipole transition $^5D_0 \rightarrow {}^7F_1$, whose intensities are almost independent of the crystal field. The peaks at 615 nm originating from the $^5D_0 \rightarrow {}^7F_2$ transition of Eu^{3+} are the hypersensitive forced electric dipole transition, whose intensities are sensitive to the local environment around Eu^{3+}. The very weak $^5D_0 \rightarrow {}^7F_3$ transitions can also be observed at 653 nm.[29] The results show that the red emission $^5D_0 \rightarrow {}^7F_2$ transition is dominant in intensity, and so, the Eu^{3+} ions mainly occupied a non-inversion symmetry center in the crystal lattice. As the concentration of Eu^{3+} increases, the emission associated with Eu^{3+} continues to increase first, and above the 3% doping concentration, it decreases due to concentration quenching. The concentration quenching effect might be due to the enhanced excitation migration or due to the activator ion coupling or coagulation.[30]

Effect of the reaction time on the PL properties of $Ba_3[Ge_2B_7O_{16}(OH)_2](OH)(H_2O):Eu^{3+}$. The excitation spectra of 3% Eu^{3+}-doped $Ba_3[Ge_2B_7O_{16}(OH)_2](OH)(H_2O):Eu^{3+}$ with hexagonal-flake morphology, recorded at an emission wavelength of 615 nm, are shown in Fig. 6 (inset). The excitation spectra exhibit a strong charge transfer band (CTB) from the 2p orbital of O^{2-} to the 4f orbital of Eu^{3+} with a maximum peak at about 242 nm. The other weak peaks are ascribed to the f–f transitions of Eu^{3+}.[28] The emission spectra (excited at 242 nm) of the 3% Eu^{3+}-doped hexagonal-flake morphology of $Ba_3[Ge_2B_7O_{16}(OH)_2](OH)(H_2O):Eu^{3+}$ prepared by varying the reaction time (24 h, 48 h, 72 h, 96 h) is shown in Fig. 6. It can be seen that the spectral shapes are similar in Fig. 5, and their assignments are the same as stated above. Upon excitation at 242 nm, the PL intensity increases with the prolonged reaction time, which may result from the improvement of crystallinity,[28] as can be observed in Fig. 1A.

Effect of the different morphologies on the PL properties of $Ba_3[Ge_2B_7O_{16}(OH)_2](OH)(H_2O):Eu^{3+}$. The excitation spectra of 3% Eu^{3+}-doped $Ba_3[Ge_2B_7O_{16}(OH)_2](OH)(H_2O):Eu^{3+}$ with hexagonal-flake morphology, recorded at an emission wavelength of 615 nm, are shown in Fig. 7 (inset). The excitation spectra exhibit a strong charge transfer band (CTB) from the 2p orbital of O^{2-} to the 4f orbital of Eu^{3+} with a maximum peak at about 242 nm. Other weak peaks are attributed to the f–f transitions of Eu^{3+}.[28] The emission spectra of 3% Eu^{3+}-doped $Ba_3[Ge_2B_7O_{16}(OH)_2](OH)(H_2O):Eu^{3+}$ prepared with different boron source raw materials under UV excitation are shown in Fig. 7. No remarkable differences in the spectroscopic characteristics of the samples with different morphologies were observed in the excitation spectra when synthesized using different boron source raw materials. The peaks at the 589 nm and 600 nm are originating from the $^5D_0 \rightarrow {}^7F_1$ transition. The peak at 615 nm is originating from the $^5D_0 \rightarrow {}^7F_2$ transition of Eu^{3+}. The very weak $^5D_0 \rightarrow {}^7F_3$ transitions can also be observed at 653 nm. The sample prepared with $Na_2B_4O_7 \cdot 10H_2O$ as the boron source (hexagonal-flake morphology) exhibited the strongest intensity. It is widely accepted that the luminescence properties of the phosphors are strongly dependent on the morphology, size, crystallinity, the center of luminescence and the density of

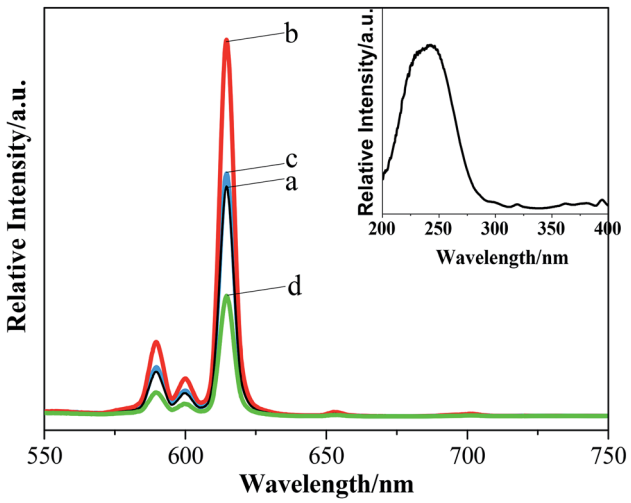

Fig. 5 The emission spectral of $Ba_3[Ge_2B_7O_{16}(OH)_2](OH)(H_2O):Eu^{3+}$ with different Eu^{3+} doping concentrations ($\lambda_{ex} = 242$ nm): (a) 1%, (b) 3%, (c) 5%, and (d) 7%.

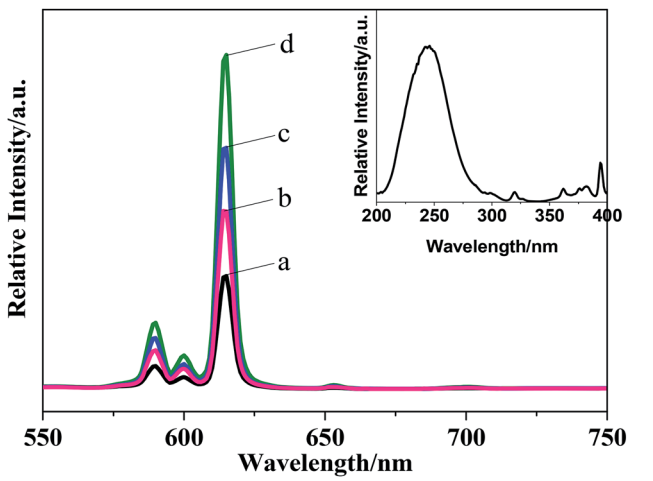

Fig. 6 The emission spectra of $Ba_3[Ge_2B_7O_{16}(OH)_2](OH)(H_2O):Eu^{3+}$ prepared for different reaction times ($\lambda_{ex} = 242$ nm): (a) 24 h, (b) 48 h, (c) 72 h, and (d) 96 h.

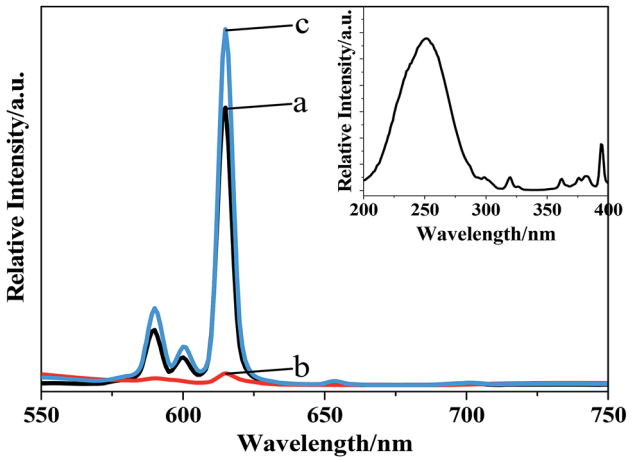

Fig. 7 The emission spectra (λ_{ex} = 242 nm) of $Ba_3[Ge_2B_7O_{16}(OH)_2]$-$(OH)(H_2O)$:$Eu^{3+}$ with different morphologies: (a) rhombohedron-like; (b) thorn-ball-like; and (c) hexagonal-flake.

defects.[18–25] The hexahedral-flake morphology of $Ba_3[Ge_2B_7$-$O_{16}(OH)_2](OH)(H_2O)$:Eu^{3+} shows the shorter edge and thickness with a larger specific surface area than the rhombohedron-like morphology and the thorn-ball-like morphology, which can result in a high concentration of luminescence centers, causing enhancement of the emission intensity.[31,32]

The photoluminescence decay curves of the samples with different morphologies $Ba_3[Ge_2B_7O_{16}(OH)_2](OH)(H_2O)$:$Eu^{3+}$ (λ_{ex} = 242 nm, λ_{em} = 616 nm) were investigated, as shown in Fig. 8. The decay curve in Fig. 8 for $Ba_3[Ge_2B_7O_{16}(OH)_2](OH)(H_2O)$:$Eu^{3+}$ can be fitted by double-exponential function as follows:

$$I = A_1 \exp(-t/\tau_1) + A_2 \exp(-t/\tau_2) \quad (1)$$

where I refers to the fluorescent intensity, A_1 and A_2 represent the constants, t is the time, and τ_1 and τ_2 correspond to the decay lifetimes of the exponential component. The double exponential fitting is attributed to the various occupied

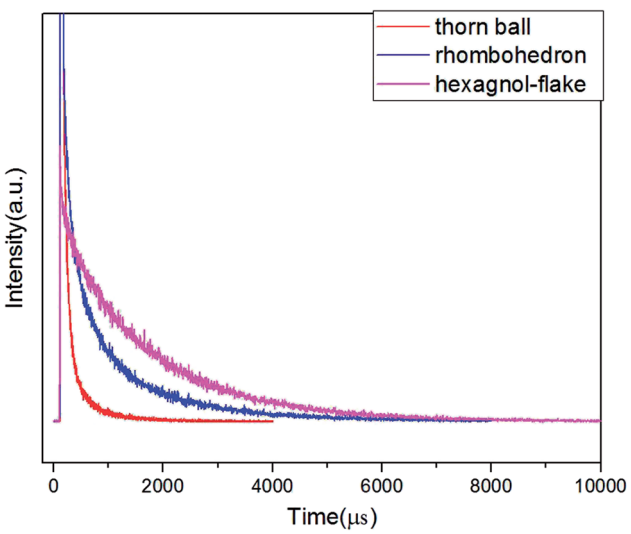

Fig. 8 The decay time curves of the investigated $Ba_3[Ge_2B_7O_{16}$-$(OH)_2](OH)(H_2O)$:Eu^{3+} with different morphologies.

positions of $Ba_3[Ge_2B_7O_{16}(OH)_2](OH)(H_2O)$:$Eu^{3+}$ phosphor. The average decay times (τ^*) can be calculated using the following equation:[33]

$$\tau^* = \left(A_1^*\tau_1^2 + I_2^*\tau_2^2\right)/\left(A_1^*\tau_1 + I_2^*\tau_2\right) \quad (2)$$

The values of the lifetime are determined to be 1.04 ms, 0.15 ms, and 1.67 ms for rhombohedron-like morphology, thorn-ball-like morphology and hexagonal-flake morphology $Ba_3[$-$Ge_2B_7O_{16}(OH)_2](OH)(H_2O)$:$Eu^{3+}$ phosphor, respectively. The lifetime is in milliseconds due to the forbidden nature of f–f transitions in Eu^{3+} ions. In addition, the hexagonal-flake morphology $Ba_3[Ge_2B_7O_{16}(OH)_2](OH)(H_2O)$:$Eu^{3+}$ phosphor possesses the longest lifetime.

The quantum yield (QY) is defined as the ratio of the number of emitted photons to the number of absorbed photons. When comparing the QY values (λ_{ex} = 394 nm) of the three morphologies of $Ba_3[Ge_2B_7O_{16}(OH)_2](OH)(H_2O)$:$Eu^{3+}$ phosphor with those of some other Eu-doped compounds reported by different authors (given in Table 1), we can see that the obtained absolute QY of the hexagonal-flake morphology $Ba_3[Ge_2B_7O_{16}$-$(OH)_2](OH)(H_2O)$:Eu^{3+} phosphor possesses the highest value (54.1%) than the rhombohedron-like morphology and thorn-ball-like morphology $Ba_3[Ge_2B_7O_{16}(OH)_2](OH)(H_2O)$:$Eu^{3+}$ phosphors. Moreover, the QY of the hexagonal-flake morphology $Ba_3[Ge_2B_7O_{16}(OH)_2](OH)(H_2O)$:$Eu^{3+}$ phosphor is equivalent to those of the $Sr_3Y_2(BO_3)_4$:Eu^{3+} powder and SrO–La_2O_3–Al_2O_3–B_2O_3–SiO_2:Eu^{3+} glass. Moreover, the QY of the hexagonal-flake morphology of $Ba_3[Ge_2B_7O_{16}(OH)_2](OH)(H_2O)$:$Eu^{3+}$ is much higher than that of the well-known commercial Y_2O_3:Eu^{3+} phosphor. Therefore, it can be concluded that the hexahedral-flake morphology $Ba_3[Ge_2B_7O_{16}(OH)_2](OH)(H_2O)$:$Eu^{3+}$ phosphor may be used as a new red phosphor for WLED.

Comparing the PL properties of $Ba_3Ge_2B_6O_{16}$:Eu^{3+} phosphor prepared by different methods. The excitation spectra of Ba_3-$Ge_2B_6O_{16}$:Eu^{3+}, recorded at an emission wavelength of 615 nm, is shown in Fig. 9A (inset). The excitation spectra exhibit a strong charge transfer band (CTB) from the 2p orbital of O^{2-} to the 4f orbital of Eu^{3+} with a maximum peak at about 242 nm. Other weak peaks are attributed to the f–f transition of Eu^{3+}.[28] The emission spectra of $Ba_3Ge_2B_6O_{16}$:Eu^{3+} phosphor prepared by the precursor method and the solid-state method are shown Fig. 9A. It can be observed that the strongest emission peak for $Ba_3Ge_2B_6O_{16}$:Eu^{3+} obtained by the precursor method was located at 614 nm, which was ascribed to red emission, and Eu^{3+} was mainly in the non-inversion center sites; meanwhile the strongest emission peak for the $Ba_3Ge_2B_6O_{16}$:Eu^{3+} obtained by high-temperature solid-state reaction was located at 591 nm, which was ascribed to orange emission, and Eu^{3+} was mainly in the inversion center sites. As shown in Fig. 9B, there are two types of surrounding environments for the Ba atoms in Ba_3-$Ge_2B_6O_{16}$, in which Ba1 is 6-coordinated by 6 O atoms, and it mainly occupies the superior symmetry site, whereas Ba2 is 7-coordinated by 7 O atoms, and it mainly occupies the inferior symmetry site.[26] Therefore, we can conclude that the Eu^{3+} occupies the Ba2 site for $Ba_3Ge_2B_6O_{16}$:Eu^{3+} obtained by the

Table 1 Quantum yield (QY) of the investigated $Ba_3[Ge_2B_7O_{16}(OH)_2](OH)(H_2O):Eu^{3+}$ with different morphologies and some other Eu-doped compounds obtained by different authors

Basic composition	QY (%)	References
$Ba_3[Ge_2B_7O_{16}(OH)_2](OH)(H_2O):Eu^{3+}$ (rhombohedron-like morphology)	50.6	This work
$Ba_3[Ge_2B_7O_{16}(OH)_2](OH)(H_2O):Eu^{3+}$ (thorn-ball-like morphology)	13.3	This work
$Ba_3[Ge_2B_7O_{16}(OH)_2](OH)(H_2O):Eu^{3+}$ (hexagonal-flake morphology)	54.1	This work
$CaB_6O_{10}:Eu^{3+}$ powder	27	34
$Sr_3Y_2(BO_3)_4:Eu^{3+}$ powder	55	35
$Li_2B_4O_7:Eu^{3+}$, Ag^+ glass	26.1	36
$Li_2B_4O_7:Eu^{3+}$ glass	10.7	37
$SrO–La_2O_3–Al_2O_3–B_2O_3–SiO_2:Eu^{3+}$ glass	54–55	38
$K_2Na_3P_3O_{10}:Eu^{3+}$ powder	14	39
$Zn_6O(OH)(BO_3)_3:Eu^{3+}$ powder	20.2	40
Commercial $Y_2O_3:Eu^{3+}$ phosphor	29.5	37

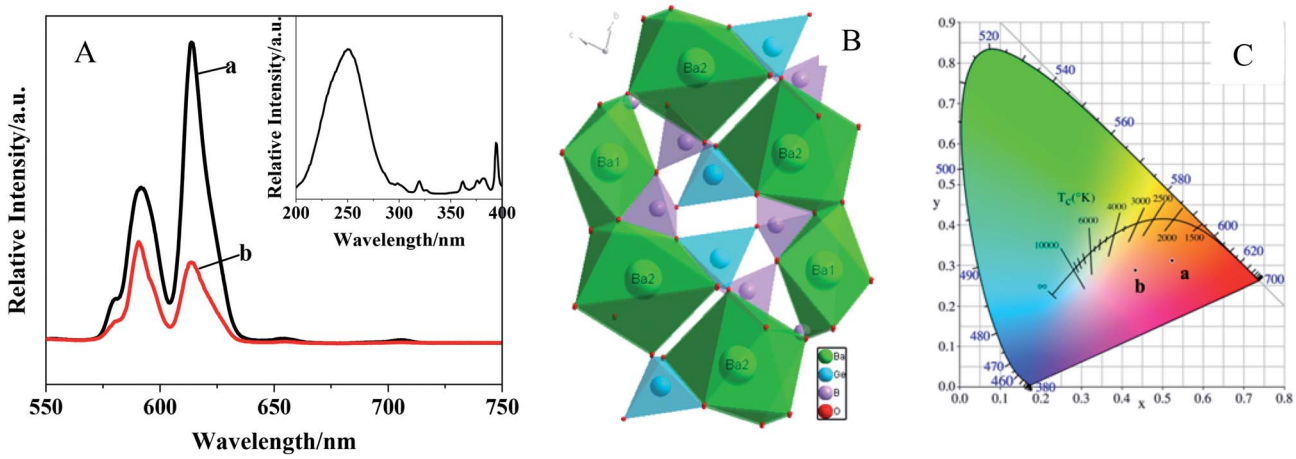

Fig. 9 (A) Emission spectra ($\lambda_{ex} = 242$ nm) of $Ba_3Ge_2B_6O_{16}:Eu^{3+}$ prepared by different reaction methods: (a) precursor method and (b) solid-state method. (B) Crystal structure of $Ba_3Ge_2B_6O_{16}$. (C) CIE chromaticity of $Ba_3Ge_2B_6O_{16}:Eu^{3+}$: (a) precursor method and (b) solid-state method.

precursor method, whereas Eu^{3+} occupies the Ba1 site for $Ba_3Ge_2B_6O_{16}:Eu^{3+}$ obtained by the high-temperature solid-state reaction. The corresponding variation in the CIE chromaticity coordinates under irradiation using a 242 nm UV lamp is demonstrated in Fig. 9C. The color tone was red (a) (0.524, 0.312) and orange (b) (0.434, 0.288) in the $Ba_3Ge_2B_6O_{16}:Eu^{3+}$ phosphors by two different preparation methods.

Conclusions

Three different morphologies of $Ba_3[Ge_2B_7O_{16}(OH)_2](OH)(H_2O):Eu^{3+}$ have been obtained by a hydrothermal reaction by varying the type of boron sources, for the first time. The effects of the doping amount of Eu^{3+}, synthetic raw materials and hydrothermal time on the luminescent properties were studied. The result indicated that the different reaction raw materials have a greater influence on the crystallinity and morphology of $Ba_3[Ge_2B_7O_{16}(OH)_2](OH)(H_2O):Eu^{3+}$, and further influence the luminescence property. The lifetime of the $Ba_3[Ge_2B_7O_{16}(OH)_2](OH)(H_2O):Eu^{3+}$ phosphor with hexagonal-flake morphology is 1.67 ms. The absolute QY of the obtained $Ba_3[Ge_2B_7O_{16}(OH)_2](OH)(H_2O):Eu^{3+}$ with hexagonal-flakes-like morphology is 54.1, which is much higher than that of the commercial $Y_2O_3:Eu$ phosphor. When the $Ba_3[Ge_2B_7O_{16}(OH)_2](OH)(H_2O):Eu^{3+}$ precursor was calcined at high temperatures, we can get $Ba_3Ge_2B_6O_{16}:Eu^{3+}$ phosphor. By comparing the luminescence properties of $Ba_3Ge_2B_6O_{16}:Eu^{3+}$ obtained by the precursor calcination method and that obtained by the high-temperature solid-state reaction, it was found that the strongest emission peak for $Ba_3Ge_2B_6O_{16}:Eu^{3+}$ obtained by the precursor calcination method appeared at 614 nm, which exhibits red emission (0.524, 0.312), meanwhile the strongest emission peak for $Ba_3Ge_2B_6O_{16}:Eu^{3+}$ obtained by the high-temperature solid-state reaction was located at 591 nm, which exhibits orange emission (0.434, 0.288).

Conflicts of interest

There are no conflicts to declare.

Acknowledgements

This work was supported by the Talent Introduction Research Project of Shaanxi Xueqian Normal University (2017DS02), the Science Foundation of Shaanxi Xueqian Normal University

(2018ZDKJ08), and the Shaanxi Provincial Department of Education Scientific Research Project (18JK0191).

Notes and references

1 L. Wu, Y. Bai, L. Wu, H. Yi, Y. Kong, Y. Zhang and J. Xu, *RSC Adv.*, 2017, **7**, 1146.
2 H. Yu, D. G. Deng, Y. J. Hua, C. X. Li and S. Q. Xu, *RSC Adv.*, 2016, **6**, 82824.
3 M. Hermus, P. C. Phan and J. Brgoch, *Chem. Mater.*, 2016, **28**, 1121.
4 H. Lin, G. Zhang, P. A. Tanner and H. Liang, *J. Phys. Chem. C*, 2013, **117**, 12769.
5 P. Liang, M. Wang and Z. H. Liu, *J. Rare Earths*, 2017, **35**, 441.
6 Y. C. Hao, C. L. Hu, X. Xu, F. Kong and J. G. Mao, *Inorg. Chem.*, 2013, **52**, 13644.
7 J. H. Zhang, F. Kong, X. Xu and J. G. Mao, *J. Solid State Chem.*, 2012, **195**, 63.
8 B. Petermüller, L. L. Petschnig, K. Wurst, G. Heymann and H. Huppertz, *Inorg. Chem.*, 2014, **53**, 9722.
9 S. J. Yu, X. Y. Gu, T. T. Deng, J. H. Huang, J. W. Cheng and G. Y. Yang, *Inorg. Chem.*, 2017, **56**, 12695.
10 R. Pan, J. W. Cheng, B. F. Yang and G. Y. Yang, *Inorg. Chem.*, 2017, **56**, 2371.
11 M. Wen, Z. Lian, H. Wu, X. Su, Q. Yan, J. Lu, Z. Yang and S. Pan, *RSC Adv.*, 2015, **5**, 53448.
12 H. Xie, M. Yue, B. Ma, D. Yang, L. Li, R. Cong, W. Gao and T. Yang, *Catal. Commun.*, 2016, **84**, 112.
13 A. Rulmont and P. Tarte, *J. Solid State Chem.*, 1988, **75**, 244.
14 S. Zhang, G. Wu, C. Duan and J. Wang, *J. Rare Earths*, 2011, **29**, 737.
15 Y. Chi, Y. Zhuang and S. P. Guo, *Z. Naturforsch., B: J. Chem. Sci.*, 2017, **72**, 95.
16 B. Knorr, K. Veenhuizen, A. Stone, H. Jain and V. Dierolf, *Opt. Mater. Express*, 2017, **7**, 4095.
17 J. H. Zhang, P. X. Li and J. G. Mao, *Dalton Trans.*, 2010, **39**, 5301.
18 P. Liang, Z. L. G. L. Tuoheti and Z. H. Liu, *RSC Adv.*, 2017, **7**, 3695.
19 Y. Zhu, Y. Liu, M. G. Brik, L. Huang, T. Xuan and J. Wang, *Opt. Mater.*, 2017, **74**, 52.
20 Y. Li, A. Zhao, C. Chen, C. Zhang, J. Zhang and G. Jia, *Dyes Pigm.*, 2018, **150**, 267.
21 P. Wang, M. Fang, M. Liu, M. Kong, W. Xu and L. Zhang, *CrystEngComm*, 2017, **19**, 5973.
22 M. Zhu, Y. Pan, Y. Huang, H. Lian and J. Lin, *J. Mater. Chem. C*, 2018, **6**, 491.
23 W. Ding, P. Liang and Z. H. Liu, *Mater. Res. Bull.*, 2017, **94**, 31.
24 D. Yue, W. Lu, C. Li, X. Zhang, C. Liu and Z. Wang, *Nanoscale*, 2014, **6**, 2137.
25 D. Zou, Y. Q. Ma, S. B. Qian, G. H. Zheng, Z. X. Dai, G. Li and M. Z. Wu, *J. Alloys Compd.*, 2013, **574**, 142.
26 J. H. Zhang, F. Kong and J. G. Mao, *Inorg. Chem.*, 2011, **50**, 3037.
27 X. Shi, L. Yuan, X. Sun, C. Chang and J. Sun, *J. Phys. Chem. C*, 12008, **12**, 3558.
28 P. Liang, J. W. Liu and Z. H. Liu, *RSC Adv.*, 2016, **6**, 89113.
29 M. Chang, Y. Song, J. Chen, L. Cui, Z. Shi, Y. Sheng and H. Zou, *ACS Sustainable Chem. Eng.*, 2018, **6**, 223.
30 P. R. Mohan, S. Gopi, V. Vidyadharan, A. George, C. Joseph, N. V. Unnikrishnan and P. R. Biju, *J. Lumin.*, 2017, **187**, 113.
31 P. Liang and Z. H. Liu, *CrystEngComm*, 2016, **18**, 1311.
32 S. W. Cao, Y. Jiao, W. F. Han, C. H. Ge, B. Song, J. Wang and X. D. Zhang, *Spectrochim. Acta, Part A*, 2018, **190**, 231.
33 A. Huang, Z. Yang, C. Yu, Z. Chai, J. Qiu and Z. Song, *J. Phys. Chem. C*, 2017, **121**, 5267.
34 K. Lemański, M. Stefański, D. Stefańska and P. J. Dereń, *J. Lumin.*, 2015, **159**, 219.
35 A. A. Shyichuk and S. Lis, *J. Rare Earths*, 2011, **29**, 1161.
36 I. I. Kindrat, B. V. Padlyak, B. Kukliński, A. Drzewiecki and V. T. Adamiv, *J. Lumin.*, 2018, **204**, 122.
37 I. I. Kindrat and B. V. Padlyak, *Opt. Mater.*, 2018, **77**, 93.
38 G. Gao and L. Wondraczek, *J. Mater. Chem. C*, 2014, **2**, 691.
39 M. Moutataouia, D. Zambon, D. Boyer, M. Lamire, L. El Ammari and R. Mahiou, *J. Alloys Compd.*, 2018, **748**, 206.
40 P. Liang, L. J. Qiao and Z. H. Liu, *Adv. Powder Technol.*, 2017, **28**, 2613.

